Interactions Between Atmospheric Pressure Plasmas and Metallic Catalyst Particles in Packed Bed Reactors

Juliusz Kruszelnicki[1], Kenneth W. Engeling[1], John E. Foster[1], and Mark J. Kushner[2,3]

[1] Nuclear Engineering and Radiological Sciences Department, University of Michigan, 2355 Bonisteel, Blvd., Ann Arbor, MI 48109-2104 USA

[2] Electrical Engineering and Computer Science Department University of Michigan, 1301 Beal Ave., Ann Arbor, MI 48109-2122 USA

[3] Author to whom correspondence should be addressed.

Email: jkrusze@umich.edu, kenengel@umich.edu, jefoster@umich.edu, mjkush@umich.edu

Abstract:

Atmospheric-pressure plasmas sustained in packed bed reactors (PBRs) are being investigated for chemical conversion of gases and pollution control. Metallic catalysts added to the surfaces of the dielectric beads of PBRs can increase the energy efficiency and selectivity of chemical processes in PBRs by reducing operating temperature and providing additional reaction pathways. In this paper, results from a computational investigation of plasma surface interactions between micron-scale metallic catalysts and humid-air plasmas in PBRs are discussed. We found that high plasma density regions form in the proximity of the metallic catalysts. These higher-density plasma regions were confirmed experimentally using ICCD imaging. The intense plasmas result from geometrical electric field enhancement and redistribution of charges within the conductive particles, leading to further enhancement. The high electric field at the triple points of the catalysts can produce field emission of electrons, which provides a pre-ionization source or additional source of electrons. These regions of high electric field and sources of electrons guide discharges towards the catalysts and increases fluxes of excited species, ions, electrons and photons to their surfaces. These fluxes are focused primarily at the triple points between the metal, dielectric and gas. As a result, the catalyst is locally heated, which could further lead to increased rates of thermocatalytic reactions on the surface. Surface roughness of the metal inclusions can lead to additional electric field enhancement, which changes the character of the discharges in the vicinity of the catalysts while reducing breakdown voltage.

Keywords: Plasma catalysis, packed bed reactor, dielectric barrier discharge, modelling

I. Introduction

Atmospheric pressure plasmas sustained in packed bed reactors (PBRs), particularly using catalysts, are being investigated for pollutant abatement and chemical conversion for production of value-added products [1]. These efforts include removal of volatile organic compounds (VOCs), NO_x abatement, CO_2 and CO chemical conversion, energy storage, and production of hydrogen, syngas, ammonia, and ozone [2–14]. There is a large variety of plasma catalytic reactors. The common feature of theses reactors is a non-equilibrium plasma being generated in near proximity of dielectric beads or granules, as in PBRs. These dielectrics are often impregnated with micro- to nanometer-scale metallic catalyst particles.

Catalysis is the process of using a material, substance or additional chemical compound to enable favorable reaction pathways by decreasing the activation energy. In spite of its industrial maturity, thermal catalysis is continually being improved. New catalysts with improved efficiencies, selectivity and turnover are being investigated experimentally and computationally [15–24]. Similarly, research is being pursued to investigate the plasma dynamics and kinetics in non-equilibrium plasma reactors in contact with catalysts, including dielectric barrier discharges (DBDs), gliding arcs, and PBRs [7,9,25–30], with support from modeling studies [31–37].

Plasma interactions with catalysts and their underlying support structures need better metrics to be able to evaluate the goodness of plasma catalysis systems and to make comparisons between systems [38–40]. Recent experimental results indicate that coupling between plasma kinetic processes and thermo-catalytic reactions leads to synergetic increases in reaction rates [26,27,41–44]. For example, Kim et al has shown a substantial increase in the production of ammonia over Ru-Mg/γ-Al_2O_3 catalyst when plasma is present [2]. This increase was greater than the sum of ammonia production when separately using plasma or thermal catalysts. Kim and colleagues also found that additional plasma formed in a DBD having dielectrics with imbedded metallic particles compared to a reactor not having metallic particles [45]. Mehta et al. investigated plasma/catalyst synergy in ammonia synthesis using microkinetics global modeling [39,46]. They postulated that the fluxes of vibrational excited nitrogen produced by the plasma could lead to a decrease in the nitrogen dissociation barrier on the surface of the catalyst and increased rates of ammonia production. Other modeling investigations have primarily focused on interactions between dielectrics and plasmas. In particular, Bogaerts et al have modeled several systems addressing plasma interactions in PBRs and with pores [47–51]. These studies empha-

sized the importance of electric field enhancement and surface charging for propagation of plasmas through systems having shaped dielectrics.

The interactions between plasma and metallic catalysts present modeling challenges due to their simultaneous and mutual impacts. The plasma produces high energy electrons, ions, excited and radical species, and UV/VUV photons [52]. The fluxes of these species can introduce additional surface kinetics (e.g., adsorption of intermediaries, UV/VUV activation), change surface morphology (e.g., sputtering, melting, self-cleaning) and increase local catalyst temperature. The electrical triple point is the intersection of a dielectric, metal and gas. Electric field enhancement occurs at triple points due to the geometry and discontinuity in permittivity, and as a response to charge-redistribution upon application of an electric field. If of sufficient magnitude, the electric field enhancement at the triple points of metallic catalyst sites can produce electric field emission of electrons, a process that is accelerated by heating of the catalyst. Electric field emission is particularly sensitive to the geometry of the metallic particles, polarization of the underlying dielectric and local plasma conditions, all of which can intensity the electric field at the surface of the catalyst. These phenomena have been studied in other areas, primarily high-voltage electrical systems [53–55]. The electric field emission in turn affects the local plasma conditions and can impact the rates of surface reactions [37]. To resolve these interactions, plasma dynamics and surface interactions must be simultaneously modeled in a self-consistent fashion.

In this work, we present results from a 2-dimensional computational investigation of the interactions between metallic particles embedded in dielectric beads and atmospheric-pressure plasmas in a PBR. The impact of size, location and topology of the metallic catalysts, as well as electric field enhancement and surface roughness, on plasma formation were studied, as well as the heating of catalyst particles by plasma-generated fluxes. We found that metallic particles embedded in the dielectrics significantly impacted plasma discharges in a PBR. In addition to geometrical electric field enhancement, charge redistribution within the conductive catalysts led to further enhancement of the electric field and higher plasma densities in their proximity. This electric field enhancement resulted in higher reactive fluxes to the catalyst, therefore increasing rates of surface reactions and energy deposition; and preferentially heating the catalysts. Electric field emission of electrons is likely to occur with moderate electric field enhancement due to roughness.

A review of the model and description of the initial conditions are in Section II. The description of the discharge dynamics in the base-case are in Section III. Sections IV and V describe the influence of electric field emission and plasma-based heating of the catalysts. Concluding remarks are in Section VI.

II. Description of the Model and Initial Conditions

The modeling platform used in this investigation was the multi-fluid plasma simulator *nonPDPSIM*, described in detail in Ref. [56]. Briefly, *nonPDPSIM* simultaneously integrates Poisson's equation (Eq.1) and continuity equations (Eq. 2) for charged and neutral species over an unstructured mesh using an implicit Newton's method. The form of Poisson's equation solved is,

$$-\nabla \cdot \varepsilon \nabla \Phi = \sum_i q_i n_i + \rho_m \tag{1}$$

where Φ is electric potential, ε is the permittivity, q_i is the charge of species i having density n_i, and ρ_M is the charge on surfaces and in materials. The continuity equation for charged particles is,

$$\frac{\partial n_i}{\partial t} = -\nabla \cdot \vec{\Gamma}_i + S_i - \left[\sum_m \nabla \cdot \vec{\Gamma}_m \gamma_m + \sum_k \nabla \cdot \vec{\varphi}_k \delta_k \right] \tag{2}$$

where Γ_i is the flux of species i. The source due to collisions is S_i. The terms in brackets only apply to electrons at boundary computational nodes adjacent to solid surfaces. At these nodes, electrons are produced by secondary electron emission (first sum) due to fluxes of ions incident onto the surface and photoemission (second sum) due to UV/VUV photons. γ_m is the secondary electron emission coefficient of species m, and δ_m is the photoelectron emission coefficient. φ_m is the flux of photon m incident onto the surface. Fluxes of charged particles are given by the Scharfetter and Gummel method that automatically provides fluxes as either upwind or downwind.

Radiation transport is performed by employing a Green's function from each node to a set of neighbors within its line-of-sight. The flux of photons between the emitting and neighboring sites decreases by the isotropic spherical expansion of the initially emitted photons, by absorption by the intervening species or by obscuration by structures. Photoionization of O_2 by

photons emitted by excited nitrogen species ($N_2(b^1\Pi)$ and $N_2(b^1\Sigma)$) was included. The non-ionizing absorption cross sections were 1×10^{-18} cm^2 for O_2 and N_2, and 3×10^{-17} cm^2 for H_2O, while the photo-ionization cross section was 1×10^{-19} cm^2.

The electron temperature is obtained by integrating an electron energy conservation equation,

$$\frac{\partial}{\partial t}\left(\frac{3}{2}n_e k_B T_e\right) = S_P\left(T_e\right) - L_P\left(T_e\right) - \nabla\cdot\left(\frac{5}{2}\vec{\Gamma}_e k_B T_e - \kappa_e\left(T_e\right)\nabla T_e\right) \tag{3}$$

where T_e is the electron temperature, n_e is the electron density, k_B is Boltzmann's constant, κ is the electron thermal conductivity, S_P is the source of power, in this case, Joule heating from the electric field and L_P represents collisional losses or gains in energy. Electron impact rate and transport coefficients are obtained from stationary solutions of Boltzmann's equation for the electron energy distribution. The ion temperatures were assumed to be equal to the gas temperature due to high rates of collisions at atmospheric pressure.

With the temperature of catalyst particles being important to their reactivity, heating of solid materials was included in the model. The gas temperature is provided by integration of

$$\frac{\partial\left(\rho c_p T_g\right)}{\partial t} = -\nabla\cdot\kappa\nabla T_g + \sum_k \frac{3}{2}n_e \nu_k\left(\frac{2m_e}{M_k}\right)k_b(T_e - T_k) - \sum_m R_m \Delta H_m\,, \tag{4}$$

where ρ is the mass density of the gas and c_p is the specific heat. The terms are for thermal conduction with thermal conductivity κ; elastic collision between electrons and heavy species having mass M_k with collision frequency ν_k; contributions from inelastic electron impact and heavy particle reactions occurring at rate R_m and having change in enthalpy ΔH_m.

The temperature of plasma facing materials is given by

$$\frac{\partial\left(\rho c_p T_m\right)}{\partial t} = -\nabla\cdot\left(-\kappa_m\nabla T_m + J_H\right), \tag{5}$$

where T_m is the material temperature, κ_m is the material thermal conductivity and J_H is the thermal heat flux (exclusive of thermal conduction) to the surface from the plasma:

$$J_H = S_i + S_e + S_n + S_{UV} \tag{6}$$

$$S_i = \sum_j \Gamma_j\left(\Phi_\lambda + \left(H_j - H_{j0}\right)\right) \tag{7}$$

$$S_e = \Gamma_e T_e - \Delta\varepsilon\left(\sum_j \Gamma_j\gamma_j + \Gamma_E\right) \tag{8}$$

$$S_n = \sum_j \Gamma_j \left(H_j - H_{jp} \right) \tag{9}$$

$$S_p = \sum_j \Gamma_j h\nu_j \left(1 - R_j \right). \tag{10}$$

In addition to thermal conduction from the plasma, heating of plasma-facing materials occurs by ion impact (S_i, Eq. 7); electron impact and (cooling by) emission of electrons (S_e, Eq. 8); exothermic and endothermic surface reactions (S_n, Eq. 9); and absorption of UV/VUV photon fluxes (S_p, Eq. 10). The heat flux by ions, S_i, has contributions from recombination of the ions with incident flux Γ_j on the surface (difference between the enthalpy of the ion H_i and its neutral counterpart, H_{io}), and the energy gained by the ion falling through the sheath potential over its mean free path, Φ. The heat flux by electrons, S_e, includes the thermal energy of the incident electrons having flux Γ_e and the cooling of the surface by electrons emitted from the surface by way of electric field emission Γ_E or secondary electron emission by ion i with probability γ_i. The secondary electrons leave the surface with $\Delta\varepsilon$= 1 eV of energy. The heat flux due to neutral species (including excited states), S_n, having incident flux Γ_n is due to the change in enthalpy of the incident particle and the products of surface reaction due to, for example, recombination of atomic or radical species, and de-excitation reactions. Photon fluxes Γ_j with energy $h\nu_j$ incident on the surface contribute heat flux S_p, de-rated by the reflection coefficient R_j.

The base case has initial conditions of 300 K and 760 Torr (or 1 atm). The gas is humid air ($N_2/O_2/H_2O$=78/21/1) with background ionization of 10^5 cm^{-3}. The reaction mechanism containing 88 species, and 1855 reactions. The reaction mechanism is a modified version of that discussed in Ref. [57] taking into account only gas-phase species.

Two geometries were used in this investigation, as shown in Figs. 1 and 2. The first geometry, Fig. 1, is nominally full scale, and includes 7 dielectric rods or disks (diameter 1.8 mm) distributed in a reactor with width of 0.8 cm, height of 1 cm. (In these 2-dimensional simulations, the circular dielectric disks are computationally equivalent to long rods.) The secondary electron emission coefficient for the dielectric is 0.15. The second geometry, Fig. 2, contains 2 dielectric rods with radii of 0.9 mm inserted into a gas region with width 0.25 cm and height of 0.29 cm. The latter geometry was used to investigate the impact of several system parameters with greater resolution of surface fluxes and of the metallic particles, while decreasing the computational costs.

In both geometries, metallic catalysts were imbedded into the surface of the dielectric rods. These catalysts are nominally electrically floating metals, which are modeled as high-conductivity dielectrics. The conductivity of the dielectric representing the catalyst particle is chosen to be high enough so that there is essentially no voltage drop across the interior of the catalyst and the interior electric field is negligible. The catalyst particles have the nominal properties of silver (work function = 5 eV, thermal conductivity = 4.06 W-cm^{-1}-K^{-1}, thermal capacity = 0.023 J-cm^{-3}-K^{-1}). The relative dielectric constant (ε_r = 10) and conductivity (σ=100 Ω^{-1}-cm^{-1}) were selected so that the dielectric relaxation time, $\tau = \varepsilon_0 \varepsilon_r / \sigma \approx 1$ fs is smaller than the smallest time-steps taken by the model ($\approx 10^{-14}$ s).

III. Plasma Propagation in PBRs with Embedded Metallic Catalyst Particles

To investigate the consequences of embedded metallic catalysts, five metallic particles were inserted flush with the surface of the top-most rod in the full scale geometry. The sizes of the catalysts varied between 15 and 50 μm. A -30 kV, 25-ns pulse was applied to the top electrode, while the bottom electrode was grounded. The location of catalysts and the voltage polarity were selected to ensure plasma formation near the metallic particles, and was based on our previous work [58,59].

Polarization of a dielectric in an external electric field can produce electric field enhancement. A cylindrical dielectric rod placed in a uniform electric field will produce electric field enhancement at the poles of the rod aligned with the electric field and will produce a reduction in electric field at the equator [48,58]. In this geometry, the vacuum electric field is not strictly vertical, however, the electric field is enhanced near the vertical poles of the rods, and minimized near their equators, as shown in Fig. 3a. With the catalysts being metal, they are equipotential and the electric field is zero inside the catalysts. This produces electric field enhancement near the triple points between the metal, dielectric and gas, as shown in Fig. 3b. At the onset of voltage, the peak E/N (electric field divided by number density) due to dielectric polarization is 245 Td (1 Td = 10^{-17} V-cm$_2$) and occurs near the top of the top-most rod. Near the catalytic particles, the E/N peaks at 295 Td. There are several locations at which the E/N is a minimum with values of approximately 65 Td, and they occur on the lateral axis between each rod pair.

The evolution of electron density, n_e, in the base case as a negative streamer develops and

propagates through the lattice of dielectric rods is shown in Fig. 4. The electron impact ionization sources, S_e, are shown in Fig. 5. First, a negative streamer propagates downward from the cathode (Fig. 4a and Fig. 5a). The streamer is directed towards the right by the polarization of the top dielectric rod which increases the electric field at the top pole of the rod. The streamer strikes and quickly charges the top surface of the rod (Fig. 5b), forming a conductive channel from the cathode to the rod (Fig. 4b). The conductive channel shorts the potential drop between the cathode and rod, which increases the polarization electric field of the adjacent rod, enabling the negative streamer to propagate in that direction. Photoionization and diffusion seeds electrons in the polarized electric field at the top of middle rod, which then enables a positive streamer to propagate upwards as a restrike (Fig. 4c and Fig. 5c). The heads of the restrike streamer are characterized by large positive charge separation ($\rho/q \approx +5 \times 10^{12}$ cm^{-3}) and electron density ($n_e=5 \times 10^{14}$ cm^{-3}), and modest electron temperatures ($T_e \approx 4$ eV). Trailing the head of the ionization wave (IW) is a largely quasi-neutral plasma column, with low electron temperature $T_e \approx 1$ eV (Figs. 4c,d; and Figs. 5c,d). The propagation of the restrike streamers is dependent on there being pre-ionization ahead of the streamer head – characteristic of positive streamers [60].

When the restrike streamers connect two dielectric rods, microdischarges form (Figs. 4e,f; and Figs 5e,f). These microdischarges have electron densities of $n_e \approx 1\times 10^{13}$ cm^{-3}. The microdischarges positively charge the surfaces of the dielectric rods, prompting development of surface ionization waves (SIWs) as shown in Fig. 5c. SIWs propagate towards the cathode, along the surface of the rods, being led by an ionization front having E/N ≈ 600 Td and $T_e \approx 7$ eV. These conditions produce a high electron impact ionization source of 5×10^{23} cm^{-3}s^{-1} leading to electron and ion densities of up to $\approx 3 \times 10^{15}$ cm^{-3} along the surface of the rods.

The impact of the metallic particles on plasma formation and propagation are shown by the enlarged insets in Figs. 4c,d, Figs. 5c,d, and in Fig. 6. As the external electric field is applied, the metal catalyst particles polarize, with charge being driven to the boundaries of the particles, increasing the geometrical electric field enhancement that occurs near the metal/dielectric/gas triple points. A small density of electrons is produced by photoionization adjacent to the catalysts, which then begin to avalanche in the electric field enhanced regions. As the positive streamer propagates upwards towards the catalysts, the vacuum electric field enhancement is further increased by the compression of electric potential due to the conductive streamer; and due to the gradient in charge density between the triple points ($\rho/q = -4\times10^{15}$ cm^{-3}) and the

streamer head ($\rho/q = +5\times10^{13}$ cm^{-3}) as shown in Figs. 6b. Directly before the streamer impacts the surface, the electric field peaks at 150 kV-cm^{-1} (610 Td) at the edge of the catalyst. This electric field is sufficient to produce electron emission (Fig. 6c). The additional electrons then serve as seed ionization for the further propagation of the streamer, and the plasma is "directed" toward the catalysts (Fig. 4c,d; Fig. 6c). The electric field emission appears to be an external source of negative charge, which produces a negative space charge region adjacent to the triple points.

Similar to non-catalytic regions, standing micro-discharges also form in the vicinity of the catalytic particles (Figs. 6c,d). With increasing conductivity adjacent to the catalysts, the electric field decreases, which in turn decreases the rate of ionization (Fig. 6d). The end result is standing microdischarges adjacent to the active catalysts – those catalysts with high enough electric field to produce electron emission. However, these microdischarges are also in regions with now low electric fields due to the high conductivity enabled by the electric field emission.

The propagation of surface ionization waves SIWs along the dielectric rods is also impacted by the catalytic particles. Due to the high conductivity of the catalysts, the electric field does not extend across the face of the particles. There is electric field enhancement at their edges, however there is no horizontal component of the electric field parallel to the face of the catalyst. As a result, propagation of SIWs stalls at the edges of each of the catalytic particles. There is insufficient horizontal component of the electric field to sustain the SIW across the metal particle.

The stalling effect is exaggerated in these simulations compared to the smaller metal particles that are used in conventional catalysts. With this simulation being 2D, the metal particles appear to be infinite stripes that go into the plane of the image. In real systems, the particles have finite width (about a unity aspect ratio) and so the SIW would likely be able to propagate around the particles while being slowed or stalled in crossing the particles. With the particles in some experimental systems approaching the nanoscale and also approaching the mean free path of electrons in the SIW, electrons might have the ability to scatter over the particle.

This stalling of SIW by catalytic particles was further investigated by re-locating the catalysts to the left equator of the dielectric rod. The electron density in the entire reactor at the end of the discharge pulse for this configuration is shown in Fig. 7a. Propagation of the SIW across the catalysts is shown in Fig. 7b. The propagation of the SIW in the absence of catalysts

is shown in Fig. 7c. In the absence of the particles, a SIW smoothly propagates upwards along the surface of the rod with a maximum electron density of nearly 10^{16} cm^{-3}. As the SIW propagates along the surface of the rod having catalyst particles and the ionization front comes in contact with the edge of a particle, the SIW stalls. The SIW is then re-initiated at the opposite edge of the particle. The re-ignition occurs due to the availability of seed electrons from photoionization resulting from VUV photons emission on the stalled side of the catalyst and by simply diffusion of electrons across the catalyst particles. These seed electrons arrive into the high electric field region at the triple point at the opposite side of the particle where E/N reaches up to ≈ 1,000 Td. Avalanche quickly occurs which restarts the SIW.

Formation of additional or higher density plasma regions near metallic catalysts has been experimentally observed by Kim et al. [45]. The authors found that the addition of silver catalysts to a zeolite packed bed reactor increased the light emission near the surfaces of the support dielectric in spots associated with the catalysts. We obtained similar results by modifying a 2-dimensional PBR previously used in experimental studies described in Refs. [58] and [59] and shown in Fig. 8a. Here, seven dielectric disks (or rods) were inserted between electrodes in a pin-to-plane configuration. Two glass plates enclosed top and bottom sides of the reactor, while ambient air flowed through the sides. A fast ICCD camera was employed to image the plasma dynamics. Silver film was applied to three locations on one of the zirconia dielectric rods, as is shown in Fig. 8a to emulate catalysts. All other experimental parameters were the same as those in discussed in Ref. [59].

A pulsed high voltage power supply was used to generate 120 ns, 20 kV pulses applied to the anode in an ambient air atmosphere. Plasma propagated from the needle electrode and through the dielectric lattice. The ICCD imaging revealed regions of intense light emission adjacent to the silver films, as shown in Fig. 8b. These brighter regions did not occur in absence of the silver films. Results from the simulation for similar conditions, shown in Fig. 8c, have high densities of light emitting excited states of N_2 adjacent to the catalysts, concurring with the experimental imaging.

IV. Influence of Electric Field Emission

The reduced geometry (Fig 2) was used to further investigate the impact of electric field enhancement and electric field emission due to the metallic catalytic particles. Electric field

emission from surfaces in the model is given by the Fowler-Nordheim expression for thermionically enhanced emission [55],

$$j_E = AT^2 \exp\left(-\left(\Phi_W - \sqrt{q^3 E/\varepsilon_0}\right)/\left(k_B T\right)\right), \tag{11}$$

where A is the Richardson-Dushman constant (120.13 A/cm^2-K^2), T is the temperature of the surface, Φ_W is the work function of the metal, k_B is Boltzmann's constant, q is the elementary charge, and E is the electric field at the surface of the metal.

Two electric field enhancement mechanisms were investigated – geometry and surface roughness. The former naturally occurs as part of the simulation. The latter was included to account for surface structures which were too small to be resolved by the numerical mesh. Surface roughness was accounted for by including a multiplicative factor to increase the electric field at the surface of the metal in Eq. 11. The electric field enhancement factor, β, has been widely used for similar purposes in other studies, particularly in the field of high voltage pulsed power [61,62]. For roughness on a metal surface, β can be estimated by

$$\beta = \frac{2\left(h/r\right)}{\ln\left(4h/r\right) - 2d}\frac{1}{d} \tag{12}$$

where h is the height of the roughness, r is the radius of curvature of its tip, and d is the distance between roughness maxima. This electric field enhancement does not penetrate into the plasma far beyond a distance equal to a few radii of curvature of the tip. As a result, β has little effect on rates of ionization in the bulk plasma further than a few microns of the surface. Electric field enhancement due to macroscopic roughness (having dimensions of hundreds of microns) would be proportionately smaller but would also penetrate further into the plasma and likely affect rates of ionization. The value of β in this investigation was varied between 1 (no enhancement) and 150 and was applied to only the metal surfaces.

First, to investigate the impact of the geometric field enhancement, the catalysts were made to protrude from the dielectric rod, as shown in Fig. 9. The electric field, ionization source and electron density are shown as the positive ionization wave approaches the catalysts. Here, a -10 kV, 5 ns pulse was applied to the top electrode. The change in geometry (flat to protruding particles) had two primary impacts. The first was to increase the initial local electric field from 120 kV-cm^{-1} to 170 kV-cm^{-1}. The second was an apparent decrease in the importance of the metal/dielectric/gas triple point. The latter was due to the location of surface charge accumula-

tion. Charge redistribution at the surface of the metal results from the applied field magnitude and direction. The topology of the surface, therefore, will impact the location of regions with highest surface charge density corresponding to the largest normal component of the electric field.

The overall evolution of the microdischarges was largely unchanged by the protrusion of the catalysts. As the positive ionization wave approached the dielectric rod having the catalysts, a high conductivity plasma column was formed. The electric field in the plasma column decreased, compressing electric potential ahead of the IW. This resulted in additional electric field enhancement at the tip of the protrusions. When the IW wave entered into this region of high electric field, the IW focused onto the protrusion, increasing the plasma density and ultimately reducing the electric field. The reduction in electric field adjacent to the protrusion increased the electric field along the neighboring surface, which enabled spread of the plasma by a SIW. The SIW then stalled at the next catalyst. The positive streamer propagation was focused toward the regions of negative surface charge, as was the case with flat catalysts. Photoionization and electron drift are responsible for seeding electrons ahead of the protruding catalysts and restarting the SIWs. The final product was a microdischarge between the rods, with an intense region of plasma at the tip of the protrusion.

Surface electric field enhancement factors, β, were then used to investigate the impact of enhancement produced by roughness that cannot be resolved in the numerical mesh. The geometry used was the same as that shown in Fig. 2. Electron densities for β values between 25 and 150 are shown in Fig. 10. For β < 10-20, there were not significant departures from the previously described discharge dynamics. For example, for β=25, electric field emission was induced from the triple-point of the middle catalyst particle. (The location of the middle catalyst particle is where the vacuum electric field is the largest due to polarization of the rods.) This catalyst became electric field-emission active as the positive IW approached the catalysts and increased the electric field in front of the IW. When the IW approached within approximately 25 μm of the surface, the electric field at the triple point increased to ≈530 kV/cm, which triggered electric field emission. As shown in Fig. 10a, this produced a filament of electron density that bridged the gap between the IW and the catalyst.

With larger values of β, the plasma became more strongly supported by surface processes. For progressively larger values of β ($50 < \beta < 75$), the electric fields adjacent to the catalysts

required to overcome the work function of the metal were produced earlier. The catalysts became active when the IW was further from the catalysts. Electric field emission transitioned from being only from the triple points of the center catalyst particle to covering the surface of the catalyst. For $\beta > 75$, electric field emission begins to occur at the triple points of the neighboring catalysts. Due to seed electrons from field emission at earlier stages of the discharge, the streamers became more directed toward the catalysts and the streamer propagation velocity increased (1×10^7 cm-s^{-1} to 3×10^8 cm-s^{-1}).

At high values of β (>100), the discharge is initially fully sustained by surface electric field emission, as in Fig. 10d. The emitted electrons initially follow the electric field lines, producing a negative, Townsend-like discharge propagating downwards. The direction of plasma propagation depends on the type of discharge formed. With low values of β, positive streamers propagate upwards between the dielectric rods. Upon approach of the positive streamer to the metal catalyst particles, which intensifies the electric field, electron emission occurs. At this point, a negative streamer may be launched but it will be weak compared to the incoming positive streamer. With high values of β, electrons emission occurs at lower electric field, which seeds a negative streamer propagating downwards. The three negative streamers are all focused towards the maximum in electric field at the pole of the lower rod where they converge.

Electric field emission requires that the metal emitting the electrons be cathodic (electrically negative) with respect to the local plasma potential. Given this requirement, the placement of the metal inclusions in this investigation was based on the particles being cathodic during the initial avalanche when electric fields are expected to be the highest. To demonstrate these principles, the reduced geometry (Fig. 2) was used to compare otherwise identical discharges but with opposite polarities. The surface roughness factor was $\beta = 10$. The electron density and charge density are shown in Fig. 11a with +10 kV applied to the bottom electrode with the top electrode being grounded. The metal inclusions are on the bottom of the top dielectric rod. The relative direction and magnitude of the electric field is the same as that in the -10 kV base case. In this configuration, the metal inclusions have a cathodic role. As the positive streamer approaches the metal particles the electric field intensifies, leading to electric field emission of electrons.

When placing +10 kV on the top electrode, the orientation of the field is reversed and the initial streamer travels in the opposite direction – as shown in Fig. 11b. (Microdischarges in

these systems tend to be initiated by positive streamers.) The metal inclusions in this configuration have an anodic role with respect to the local plasma potential, polarizing charge to be positive along the surface of the particle. As plasma forms, the high current of electrons to those surfaces neutralizes and then charges them negatively. As the streamer approaches the lower dielectric rod, compression of the potential intensifies the electric field at the surface, directly analogous to the opposite polarity near the metal inclusions. Had metal inclusions been placed on the plasma facing surface of the bottom rod, electric field emission would have occurred in the same manner as the opposite polarity on the top dielectric rod.

The outcome of these studies is that electric field emission will occur in PBRs independent of the applied polarity as long as the metal inclusions have a geometrical orientation that places them in a cathodic role when the local electric field intensifies to sufficient magnitude. Metal inclusions on the bottom side of a dielectric rod serving in an anodic role will not produce electric emission. Inclusions on the opposite side of the rod which are geometrically positioned in a cathodic role may produce electric field emission even if the applied polarity is positive.

The practical implications of these phenomena are several. Polarization of metallic particles result in guiding of streamers towards the catalysts, leading to preferential rates of interaction between catalysts and plasma products. The resulting electric-field emission of electrons can lead to increased plasma volumes and plasma/catalyst interactions, and potentially explains additional plasma formation observed in experiments. Simultaneously, the increases in electric field emission can serve to decrease local, transient charge gradients, therefore reducing instantaneous electric fields and cooling electrons near the catalyst surfaces. Variation in electron temperature can, then, affect the local gas kinetics, and provide an additional pathway to catalytic selectivity.

The electric field at the surface of the catalyst determines the onset of the field emission. Sustaining that field emission depends on being able to sustain this critical electric field, which becomes progressively more difficult as conductive plasma forms in front of the catalyst particle. Even if this electric field could be sustained, the total amount of electric field emission would ultimately be limited by the capacitance of the particle. In electric field emission from, for example, an electrode connected to a power supply, there is a nearly unlimited amount of current that can be emitted. Electrons emitted from the surface of the metal are replaced by electrons from the power supply. The power supply may itself have a finite capacitance but, in principle,

the electron source is not limited. In a PBR, the catalyst particles are electrically floating bodies whose ability to deliver charge is limited by their capacitance – the catalyst will stop emitting when its capacitance has been charged to the degree that the electric field at its surface decreases. This charging process is influenced by the displacement current that can be delivered to the back side of the catalyst through the dielectric in which the catalyst is embedded, the size of the particle and the conductivity of the plasma by the particle.

V. Fluences of Reactive Species and Impact on Catalyst Temperature

While the catalysts can have a large impact on the dynamics of the discharge, the reverse is also true. The plasma can heat the catalysts, increasing the rates of some thermostatic reactions. Fluxes of energetic UV photons, electrons and ions can clean contaminants from surface sites; and high applied electric fields can decrease potential energy barriers of surface reactions. Only a subset of these phenomena could be investigated in this work – fluences of reactive species and the heating rates.

The fluences of selected plasma produced species and photons to the surfaces of the catalysts in the reduced geometry as a function of β are shown in Fig. 12. These fluxes are integrated over the surface of the center catalytic particle. As β increased, the fluences of all ions, radical, photons and electrons decreased. This result, while counter-intuitive, is explained by the shorting of the electric field in the gas gap by the conductive plasma enabled by high β. In the instant that electric emission begins, there is an increase in production of all ions, radicals, photons and electrons. The electric field is large and so electron impact rate coefficients are also large. However, as the number of electric field emitted electrons near surfaces increases, the electric field in the plasma decreases and the local electron temperature decreases, causing the rates of electron-impact reactions to also decrease. The relative rates of reactions having higher threshold energies decreased more quickly with increasing β. For example, the electron impact dissociation of N_2 has a higher threshold energy ($\approx$ 12 eV) than that for O_2 ($\approx$ 5 eV). As a result, the fluence of atomic nitrogen onto the catalysts decreases more rapidly than the fluence of atomic oxygen. This effect could be used to tune the species that adsorb onto and react with catalysts.

Power deposition onto the surface of the catalyst results from reactions of neutral species, UV fluxes, kinetic energy of charged species, and the ionization potential of incident ions, as described in Section II. The power deposition onto the surface of the catalyst and the fractional

contribution to heating the catalyst due to electrons, ions, and neutrals are shown in Fig. 13 for β = 10. The contribution from UV photons is small. At the beginning of the discharge (t < 1.5 ns), the majority of heating is by electrons, though the absolute magnitude of that heating is small. Once a streamer forms and makes contact with the surface, the total energy deposition increases by two orders of magnitude due to power deposition by ions which carry with them their ionization potential as well as kinetic energy due to the local electric field. With increasing dissociation of the gas adjacent to the particle, neutral reactions on the surface of the particles also begin to heat the particles. The heating of the particles, up to 60 kW/cm^2, occurs over about 1 ns, dominated by ion impact. In the post-pulse period (t > 3 ns), the heating by ions decreases as the plasma dissipates while power deposition continues due to surface reactions of the neutral species. Heating of the particles by surface reactions will continue as long as there are radicals diffusing to the particle.

The total amount of energy deposited onto the surface of the catalyst per pulse is not large, however the particles are small. The energy deposition per pulse is about 10 μJ/cm^2. The heating of the particle is then determined by the repetition rate of the discharge and the thermal conductivity of the dielectric in which the particle is embedded. To model the heating of the catalyst, the temperature equation was integrated while providing impulsive increments of surface energy (as would be delivered by the discharge). The energy source terms as a function of position on the catalyst from the first pulse were recorded and inserted as a delta function at a frequency of 10 kHz. Heat conduction and convection equations were solved throughout the reduced computational domain while having a constant temperature (300 K) boundary condition on the walls of the reactor. Over the equivalent of 150,000 pulses (15 seconds at 10 kHz), the temperature of the catalyst increased to ≈500 K before reaching a quasi-equilibrium. This increase of 200 K is high enough to impact rates of thermocatalytic reactions. Since the streamers were focused on the triple points, energy deposition and temperature increases were not uniform. Rather, the temperatures first increased at those locations. Thermal conduction then spread the higher temperature throughout the rest of the solid – metal and dielectric alike.

VI. Concluding Remarks

Interactions between atmospheric-pressure plasmas and metallic catalysts in a packed-bed reactor were computationally investigated. In addition to geometrical electric field en-

hancement, the metallic particles produced further local electric field enhancement due to redistribution of charges in the particles. As a result, discharges were guided towards the metallic particles, and higher density plasma formed in the proximity of their surfaces. Formation of additional plasma near the catalysts therefore led to higher fluxes of reactive species to their surfaces which could, in part, produce an increase the efficiency of atmospheric pressure plasma based catalysis. The geometrical electric field enhancement was intensified by the space-charge gradient between streamer heads and the particles, leading to electric-field emission of electrons. These effects then led to a decrease in the voltage required to reach breakdown when compared to the same reactor without metallic particles.

An electric field enhancement factor, β, was used as a proxy for enhancement that occurs due to surface roughness that could not be resolved in the numerical mesh. Increasing β and increasing the local electric field produced rapid increase in electric field emission. This field emission enabled formation of plasma in regions where discharges would not otherwise occur, leading to larger total plasma volume. However, higher β also resulted in a decrease in local electric fields once plasma formed due to the additional source of electrons near the surface. This change in electric field in the plasma changed the selectivity of plasma produced reactive species formed near the catalysts. Plasma-produced species were preferentially focused onto the surface in the vicinity of the catalyst, resulting in preferential heating of the particles that would directly affect thermally sensitive chemical processes.

During review of this paper, a referee asked about electric field emission that might occur from the dielectric support due to surface roughness represented by a β factor. Dielectrics do emit electrons following ion bombardment with secondary emission coefficients, γ, as large as 0.15 [63]. Dielectrics undergo photo-electron emission [64], though the emission may be transient due to the resulting positive charging of the surface. Dielectrics have work functions. As a result there will be some form electric field emission, which will be very sensitive to the resulting positive charging of the surface [65] In metals, this positive charging is neutralized by electron current from within the metal. Thin films of dielectrics over metals are able to continuously emit electrons as the metal injects electrons into the dielectric, which then traverse the thin insulator. Thick dielectrics only transiently emit due to this surface charging. Simulations of our PBR reactor were performed for the base case while applying the expression for metal electric field emission (Eq. 11) to the surface of the dielectric rods (β = 100). This expression likely

greatly over-estimates the emitted current. Electric field emission did occur from the dielectric only near the metal inclusions where there was already physical electric field enhancement, while surface charging eventually diminished the emission. Due to the thickness dependence of electron emission from dielectrics, the fact that dielectrics in these systems are typically not in electrical contact with metals except at isolated points, and the unrealistically large values β that would likely be required, we do not expect that electric field emission from dielectrics of the type found in PBRs will be important.

Different metal catalysts produce significant differences in chemical processing. However, the electrical processes discussed here will apply to all types of metal particles. For example, the tendency for metal inclusions to block propagation of surface ionization waves will depend only weakly on the type of metal as the conductivity of all metals is large enough to produce the blockage. The greatest sensitivity to the type of metal will be through the work function of the metal. Larger work functions will require larger electric fields to produce significant electric field emission. The work functions of most metals are between 4-5 eV [66]. Inclusions with component metals having lower work functions, for example Ce [2.9 eV], Ba [2.52 eV] or Mg [3.66 eV], would be more sensitive to electric emission due to the onset of their emission occurring at lower electric fields. Inclusions with component metals having exposed crystallographic planes with higher work functions, for example Co [5.0 eV], W [5.22 eV] or Pt [5.2-5.9 eV], would be less sensitive to electric field emission.

Data Availability

The data that support the findings of this study are available from the corresponding author upon reasonable request.

Acknowledgements

This material was based upon work supported by the U.S. Department of Energy, Office of Science, Office of Fusion Energy Sciences under award numbers DE-SC000319 and DE-SC0020232, and the National Science Foundation (PHY-1902878).

Figure Captions:

1. Geometry of the base case reactor. (a) Schematic of the entire reactor. b) computational mesh, c) enlargement of the topmost disk and d) enlargement of numerical mesh.
2. Geometry of the reduced scale reactor. (a) Schematic of the entire reactor. b) computational mesh, c) enlargement of inter-disk gap and catalysts and d) enlargement of numerical mesh.
3. Reduced electric field (E/N) at t = 0 s for a) the full-size base-case geometry and b) enlargement near the catalysts.
4. Time evolution of electron density in the full-size base-case. a) 3.0 ns, b) 10.8 ns, c) 12.8 ns, d) 14.2 ns, e) 15.4 ns and f) 16.5 ns. At each time, images are shown for the (left) full reactor and (right) enlargements in regions of interests. Densities are plotted on a 4-decade log scale with the maximum value indicated in each frame.
5. Time evolution of electron impact source time in the full-size base-case. a) 2.0 ns, b) 3.5 ns, c) 11.6 ns, d) 11.9 ns, e) 13.9 ns and f) 15.8 ns. At each time, images are shown for the (left) full reactor and (right) enlargements in regions of interests. Sources are plotted on a 4-decade log scale with the maximum value indicated in each frame.
6. Plasma properties in the vicinity of the catalyst particles (left to right) electric field, charge density, ionization source term and electron density at times of a) 11.7 ns, b) 11.9 ns, c) 12.1 ns and d) 12.3 ns. These images are during streamer propagation toward the metallic catalysts. Gradients in charge density lead to formation of strong electric fields, and electric field emission of electrons from the surfaces of metals.
7. Electron density in the full-size geometry with catalysts arranged along the left pole of the topmost particle. a). Electron density in entire reactor at 16.3 ns. b) Surface ionization wave (SIW) in the vicinity of the catalysts (15.6 ns to 16.9 ns) showing stagnation of SIWs approaching the catalysts and re-ignition on the other side. c) SIW for the same location without metallic catalysts. Densities are plotted on a 4-decade log scale.
8. Experimental and computational comparison. a) Schematic experimental set-up of 2-dimensional packed bed reactor with silver film placed on top right dielectric disk. b) ICCD image of plasma emission near silver film. c) Computed densities of light-emitting species in a similar system.
9. Plasma properties in the vicinity of protruding catalytic particles (left to right) electric field, electron impact ionization source and electron density at times of a) 0.4 ns, b) 0.6 ns, c) 0.8 ns and d) 0.8 ns. Electron density and source are plotted on a 3 decade log scale unless indicated otherwise. The maximum values or range of values plotted in each are indicated in each frame.
10. Electron densities at the end of the voltage pulse for different values of the electric field enhancement factor, β, in the reduced geometry at different times (left to right). β = a) 25, b)

50, c) 75 and d) 150. Densities are plotted on a 4-decade log-scale with maximum values noted in each frame. The mechanism of plasma formation changes from being volume to surface dominated with increasing β,

11. Electron density and charge density in positive-voltage cases where a) the top electrode is powered and b) the bottom electrode is powered. Both densities are plotted on a 4-decade log-scale. The charge density shows both negative and positive values. The discharge properties and effects of the catalysts are dependent on whether the metal inclusions serve in a cathodic role and not necessarily on the polarity of the pulse.

12. Fluences of selected species to the surfaces of the middle catalyst particle as a function of electric field enhancement factor for the reduced-scale geometry. a) O, OH, H, N and b) N_2^+, O_2^+, UV photons and electrons. With the increase in conductivity due to electric field emission of electrons, the electric field in the adjacent plasma decreases, leading to a colder plasma and decreased fluences to the surface.

13. Total and fractional power deposition to surface of catalyst as a function of time for the reduced scale geometry base case. Power deposition by ions dominates, with neutral chemical reactions dominating in the afterglow.

References

[1] H. Kim, Y. Teramoto, A. Ogata, H. Takagi and T. Nanba, Plasma Process. Polym. **36,** 45 (2016).

[2] H.-H. Kim, Y. Teramoto, A. Ogata, H. Takagi and T. Nanba, Plasma Chem. Plasma Process. (2015).

[3] J. Hong, S. Prawer and A. B. Murphy, ACS Sustain. Chem. Eng. **6,** 15 (2018).

[4] B. S. Patil, Q. Wang, V. Hessel and J. Lang, Catal. Today **256,** 49 (2015).

[5] A. Bogaerts and E. C. Neyts, ACS Energy Lett. **3,** 1013 (2018).

[6] R. Brandenburg, A. Bogaerts, W. Bongers, A. Fridman, G. Fridman, B. R. Locke, V. Miller, S. Reuter, M. Schiorlin, T. Verreycken and K. K. Ostrikov, Plasma Process. Polym. **16,** 1700238 (2017).

[7] X. Tu, H. J. Gallon, M. V Twigg, P. a Gorry and J. C. Whitehead, J. Phys. D. Appl. Phys. **44,** 274007 (2011).

[8] Y. X. Zeng, L. Wang, C. F. Wu, J. Q. Wang, B. X. Shen and X. Tu, Appl. Catal. B Environ. **224,** 469 (2018).

[9] U. Roland, F. Holzer and F. D. Kopinke, in Catalysis Today **73,** 315 (2002).

[10] W. Chung and M. Chang, Renew. Sustain. Energy Rev. **62,** 13 (2016).

[11] G. J. van Rooij, D. C. M. van den Bekerom, N. den Harder, T. Minea, G. Berden, W. A. Bongers, R. Engeln, M. F. Graswinckel, E. Zoethout and M. C. M. van de Sanden, Faraday Discuss. **183,** 233 (2015).

[12] A. Bogaerts, T. Kozák, K. van Laer and R. Snoeckx, Faraday Discuss. 217 (2015).

[13] I. Michielsen, Y. Uytdenhouwen, J. Pype, B. Michielsen, J. Mertens, F. Reniers, V. Meynen and A. Bogaerts, Chem. Eng. J. **326,** 477 (2017).

[14] H. H. Kim, Y. Teramoto, A. Ogata, H. Takagi and T. Nanba, Plasma Process. Polym. **14,** 1600157 (2016).

[15] M. Besora and F. Maseras, WIREs Comput. Mol. Sci. **8,** 1372 (2018).

[16] H. Liu, Chinese J. Catal. **35,** 1619 (2014).

[17] A. Bogaerts, X. Tu, J. C. Whitehead, G. Centi, L. Lefferts, O. Guaitella, F. Azzolina-Jury, H. Kim, A. B. Murphy, W. F. Schneider, T. Nozaki, J. C. Hicks, A. Rousseau, F. Thevenet, A. Khacef and M. Carreon, J. Phys. D Appl. Phys. **53,** (2020).

[18] R. Snoeckx and A. Bogaerts, Chemi. Soc. Rev. **46,** (2017).

[19] S. Xu, S. Chansai, C. Stere, B. Inceesungvorn, A. Goguet, K. Wangkawong, S. F. R. Taylor, N. Al-Janabi, C. Hardacre, P. A. Martin and X. Fan, Nat. Catal. **2,** 142 (2019).

[20] R. Gholami, C. E. Stere, A. Goguet and C. Hardacre, Phil. Trans. R. Soc. A **376,** 20170054 (2017).

[21] J. G. Chen, R. M. Crooks, L. C. Seefeldt, K. L. Bren, R. Morris Bullock, M. Y. Darensbourg, P. L. Holland, B. Hoffman, M. J. Janik, A. K. Jones, M. G. Kanatzidis, P. King, K. M. Lancaster, S. V. Lymar, P. Pfromm, W. F. Schneider and R. R. Schrock, Science (80-.). **360,** 873 (2018).

[22] H. Puliyalil, D. Lašič Jurković, V. D. B. C. Dasireddy and B. Likozar, RSC Adv **8,** 27481 (2018).

[23] S. Liu, L. R. Winter and J. G. Chen, ACS Catal. **10,** 2855 (2020).

[24] Z. Wang, Y. Zhang, E. C. Neyts, X. Cao, X. Zhang, B. W. L. Jang and C. J. Liu, ACS Catal. **8,** 2093 (2018).

[25] A. Vesel, M. Mozetic, A. Drenik and M. Balat-Pichelin, Chem. Phys. **382,** 127 (2011).

[26] H. Lee, D.-H. Lee, Y.-H. Song, W. C. Choi, Y.-K. Park and D. H. Kim, Chem. Eng. J. **259,** 761 (2015).

[27] F. Holzer, F. D. Kopinke and U. Roland, Plasma Chemistry and Plasma Processing **25,** 595 (2005).

[28] T. Nunnally, K. Gustol, A. Rabinovich, A. Fridman, A. Gustol and A. Kemoun, J. Phys. D Appl. Phys. **44,** 274009 (2011).

[29] K. Hensel, Eur. Phys. J. D. **54,** 141 (2009).

[30] K. Hensel, V. Martišovitš, Z. Machala, M. Janda, M. Leštinský, P. Tardiveau and A. Mizuno, Plasma Process. Polym. **4,** 682 (2007).

[31] E. C. Neyts and A. Bogaerts, J. Phys. D. Appl. Phys. **47,** 224010 (2014).

[32] P. Brault, J. M. Bauchire, F. James and C. Josserand, Defect Diffus. Forum **323–325,** 387 (2012).

[33] A. Bogaerts, Q. Z. Zhang, Y. R. Zhang, K. Van Laer and W. Wang, Catal. Today **337,** 3 (2019).

[34] J. Hong, S. Pancheshnyi, E. Tam, J. J. Lowke, S. Prawer and A. B. Murphy, J. Phys. D Appl. Phys. **51,** 109501 (2018).

[35] S. Matera, W. F. Schneider, A. Heyden and A. Savara, ACS Catal. **9,** 6624 (2019).

[36] A. Bogaerts, A. Berthelot, S. Heijkers, S. Kolev, R. Snoeckx, S. Sun, G. Trenchev, K. Van Laer and W. Wang, Plasma Sources Sci. Technol. **26,** 063001 (2017).

[37] F. Che, J. T. Gray, S. Ha, N. Kruse, S. L. Scott and J. S. McEwen, ACS Catal. **8,** 5153 (2018).

[38] J. C. Whitehead, J. Phys. D Appl. Phys. **49,** 243001 (2016).

[39] P. Mehta, P. Barboun, D. B. Go, J. C. Hicks and W. F. Schneider, ACS Energy Lett. **4,** 1115 (2019).

[40] S. Tanaka, H. Uyama and O. Matsumoto, Plasma Chem Plasma Process **14,** 4 (1994).

[41] E. C. Neyts, K. K. Ostrikov, M. K. Sunkara and A. Bogaerts, Chem. Rev. **115,** 13408 (2015).

[42] F. A. Herrera, G. H. Brown, P. Barboun, N. Turan, P. Mehta, W. F. Schneider, J. C. Hicks and D. B. Go, J. Phys. D Appl. Phys. **52,** 224002 (2019).

[43] L. F. Spencer and A. D. Gallimore, Plasma Sources Sci. Technol. **22,** 015019 (2013).

[44] L. Di, J. Zhang, M. Craven, Y. Wang, H. Wang, X. Zhang and X. Tu, Catal. Sci. Technol. **10,** 6129 (2020).

[45] H. H. Kim and A. Ogata, Eur. Phys. J. Appl. Phys. **55,** 13806 (2011).

[46] P. Mehta, P. Barboun, F. A. Herrera, J. Kim, P. Rumbach, D. B. Go, J. C. Hicks and W. F.

Schneider, Nat. Catal. **1,** 269 (2018).

[47] K. Van Laer and A. Bogaerts, Plasma Sources Sci. Technol. **26,** 085007 (2017).

[48] K. Van Laer, S. Kolev and A. Bogaerts, Plasma Sources Sci. Technol. **25,** 015002 (2015).

[49] W. Wang, H. H. Kim, K. Van Laer and A. Bogaerts, Chem. Eng. J. **334,** 2467 (2018).

[50] Q. Z. Zhang and A. Bogaerts, Plasma Sources Sci. Technol. **27,** 105013 (2018).

[51] Y. R. Zhang, K. Van Laer, E. C. Neyts and A. Bogaerts, Appl. Catal. B Environ. **185,** 56 (2016).

[52] D. Mei, X. Zhu, C. Wu, B. Ashford, P. T. Williams and X. Tu, Appl. Catal. B Environ. **182,** 525 (2016).

[53] A. M. Darr, A. M. Loveless and A. L. Garner, Appl. Phys. Lett. **114,** 014103 (2019).

[54] F. Schertz, M. Schmelzeisen, M. Kreiter, H. Elmers and G. Schönhense, Physi. Rev. Let. **108,** 237602 (2012).

[55] R. G. Forbes, J. Vac. Sci. Technol. B **26,** 2 (2008).

[56] S. A. Norberg, E. Johnsen and M. J. Kushner, Plasma Sources Sci. Technol. **24,** 035026 (2015).

[57] A. M. Lietz and M. J. Kushner, J. Phys. D. Appl. Phys. **49,** 425204 (2016).

[58] J. Kruszelnicki, K. W. Engeling, J. E. Foster, Z. Xiong and M. J. Kushner, J. Phys. D Appl. Phys. **50,** 025203 (2017).

[59] K. W. Engeling, J. Kruszelnicki, M. J. Kushner and J. E. Foster, Plasma Sources Sci. Technol. **27,** 085002 (2018).

[60] S. Nijdam, J. Teunissen, E. Takahashi and U. Ebert, Plasma Sources Sci. Technol. **25,** 044001 (2016).

[61] R. C. Smith, R. D. Forrest, J. D. Carey, W. K. Hsu and S. R. P. Silva, Appl. Phys. Lett. **87,** 013111 (2005).

[62] Z. Xu, X. D. Bai and E. G. Wang, Appl. Phys. Lett. **88,** 133107 (2006)

[63] G. Auday, Ph. Guillot, and J. Galy. J. Appl. Phys. **88**, 4871 (2000).

[64] J. L. Lauer, J. L. Shohet and R. W. Hansen, J. Vac. Sci. Technol. A **21**, 1253 (2003).

[65] J. C. Schug, A. C. Lilly and D. A. Lowitz, Phys. Rev. B **1**, 4811 (1970).

[66] https://public.wsu.edu/~pchemlab/documents/Work-functionvalues.pdf.

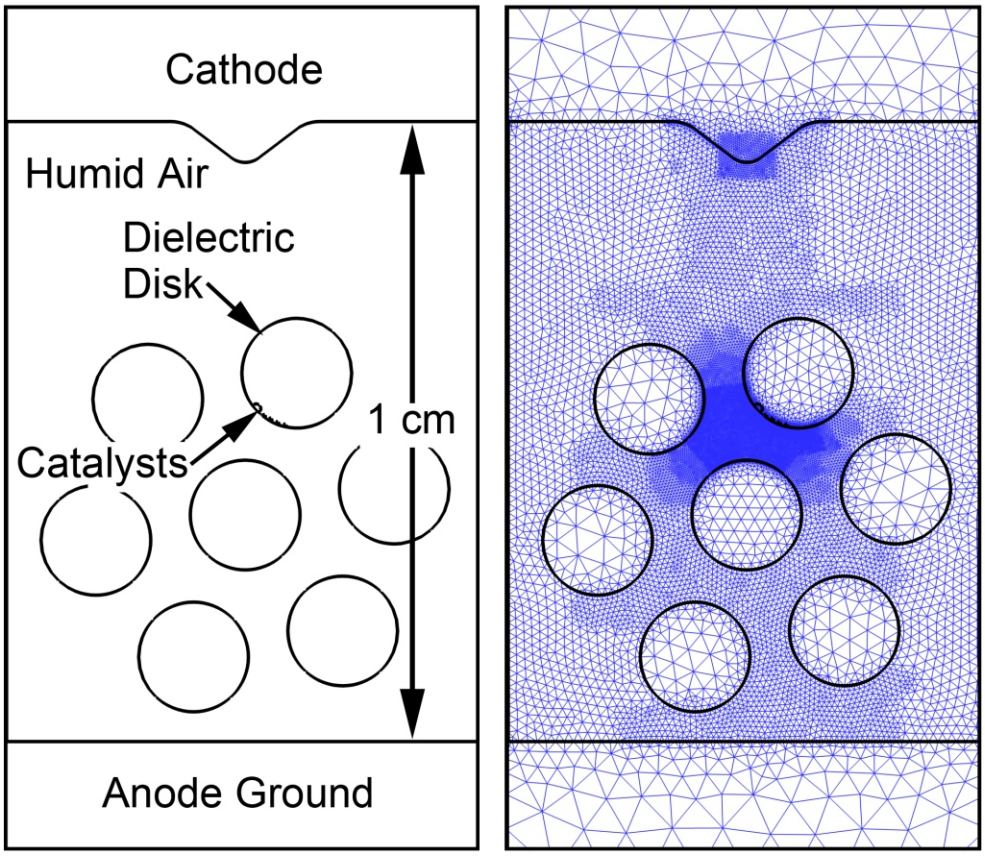
Cathode
Humid Air
Dielectric
Disk
Catalysts
1 cm
Anode Ground
a)
b)
1.8 mm
50 μm
c)
d)

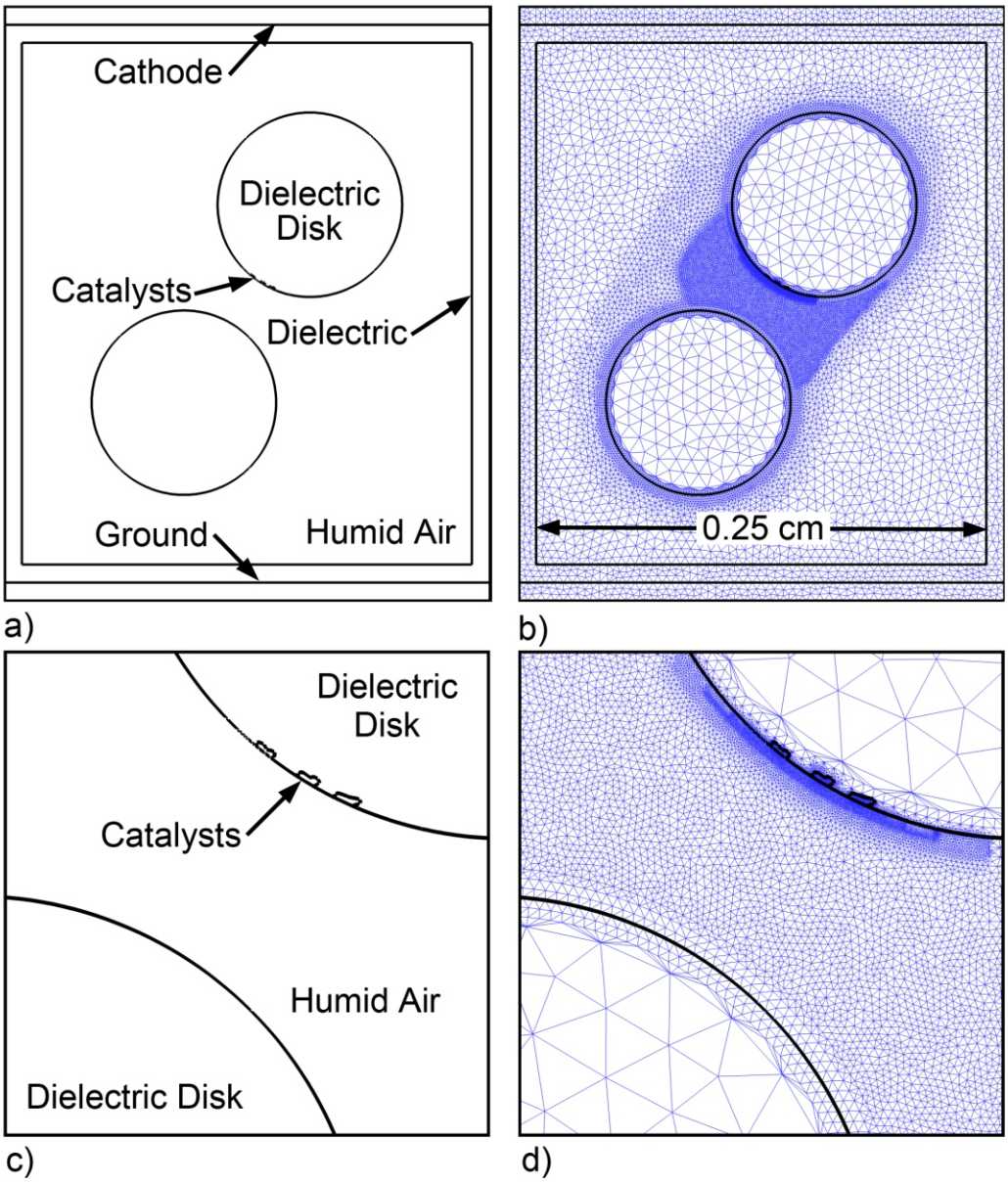
Cathode
Dielectric Disk
Catalysts
Dielectric
Ground
Humid Air
a)
0.25 cm
b)
Dielectric Disk
Catalysts
Humid Air
Dielectric Disk
c)
d)

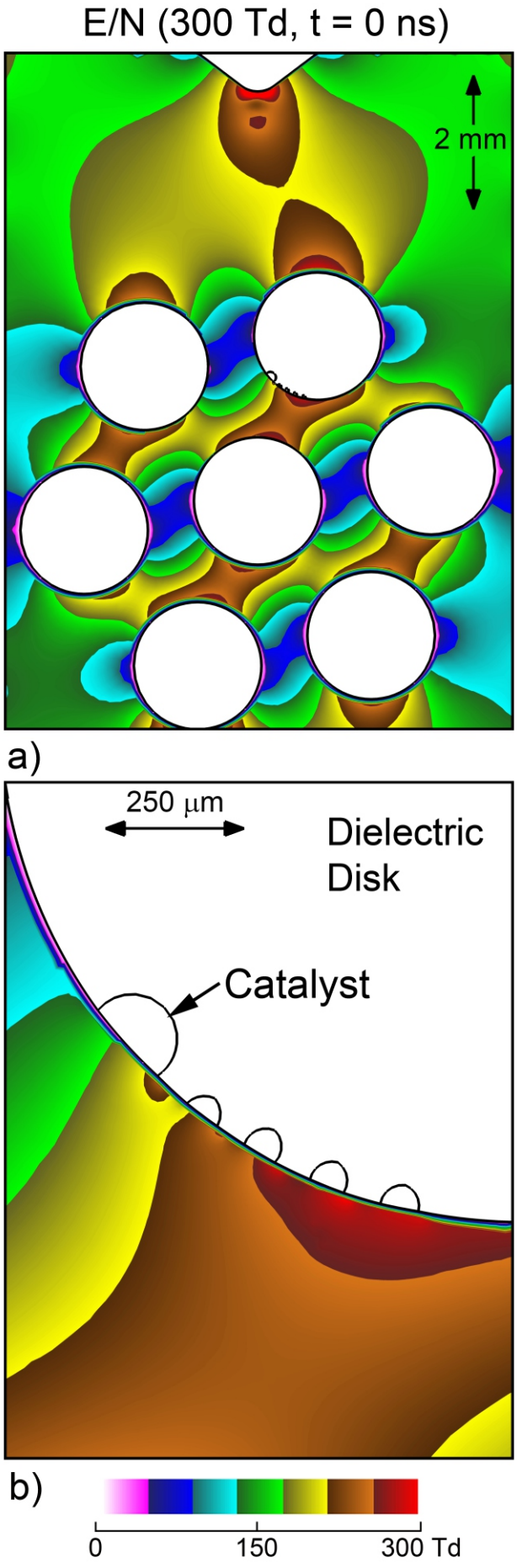

Kruszelnicki et al.
Figure 3 of 13

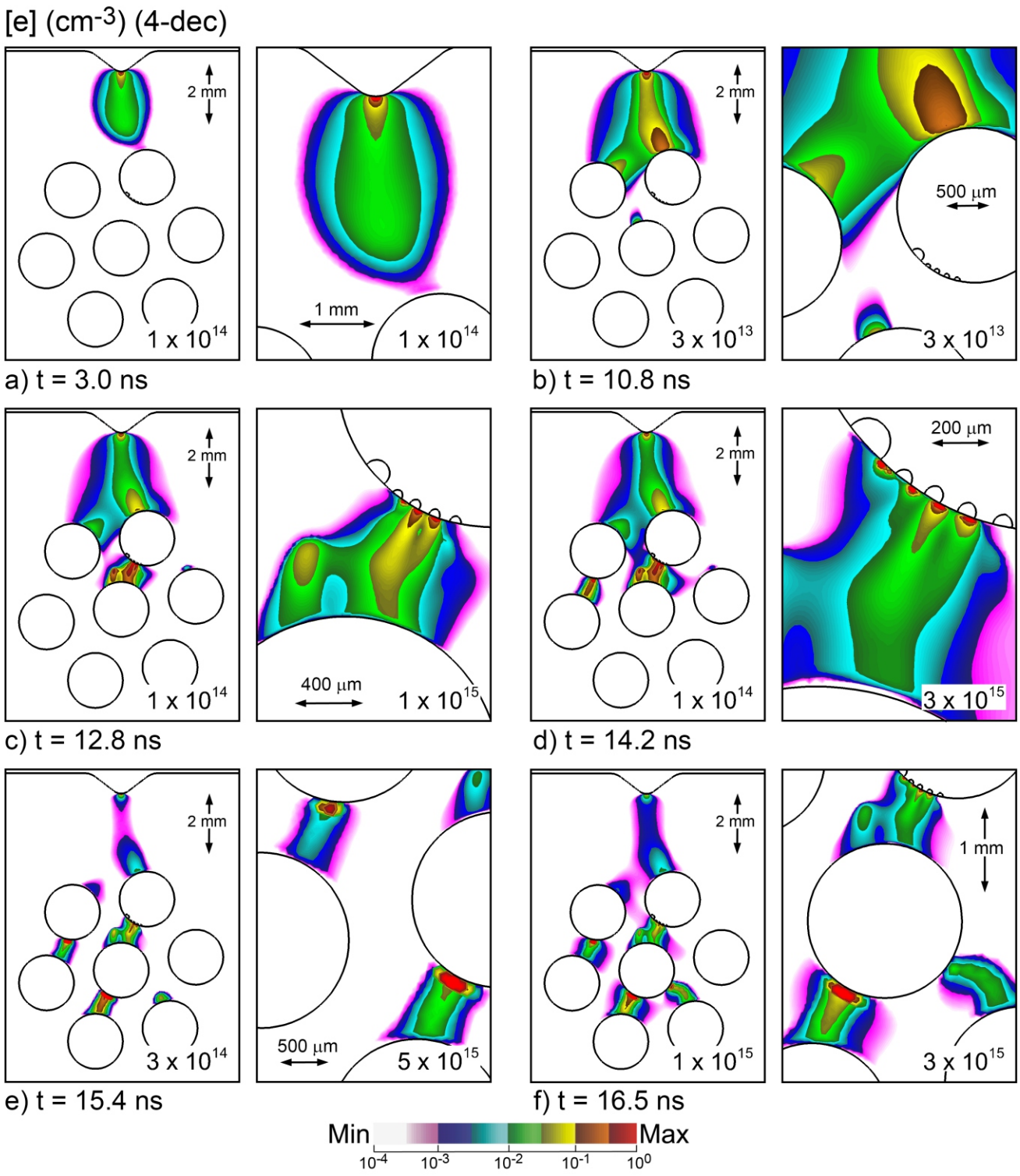

Kruszelnicki et al.
Figure 4 of 13

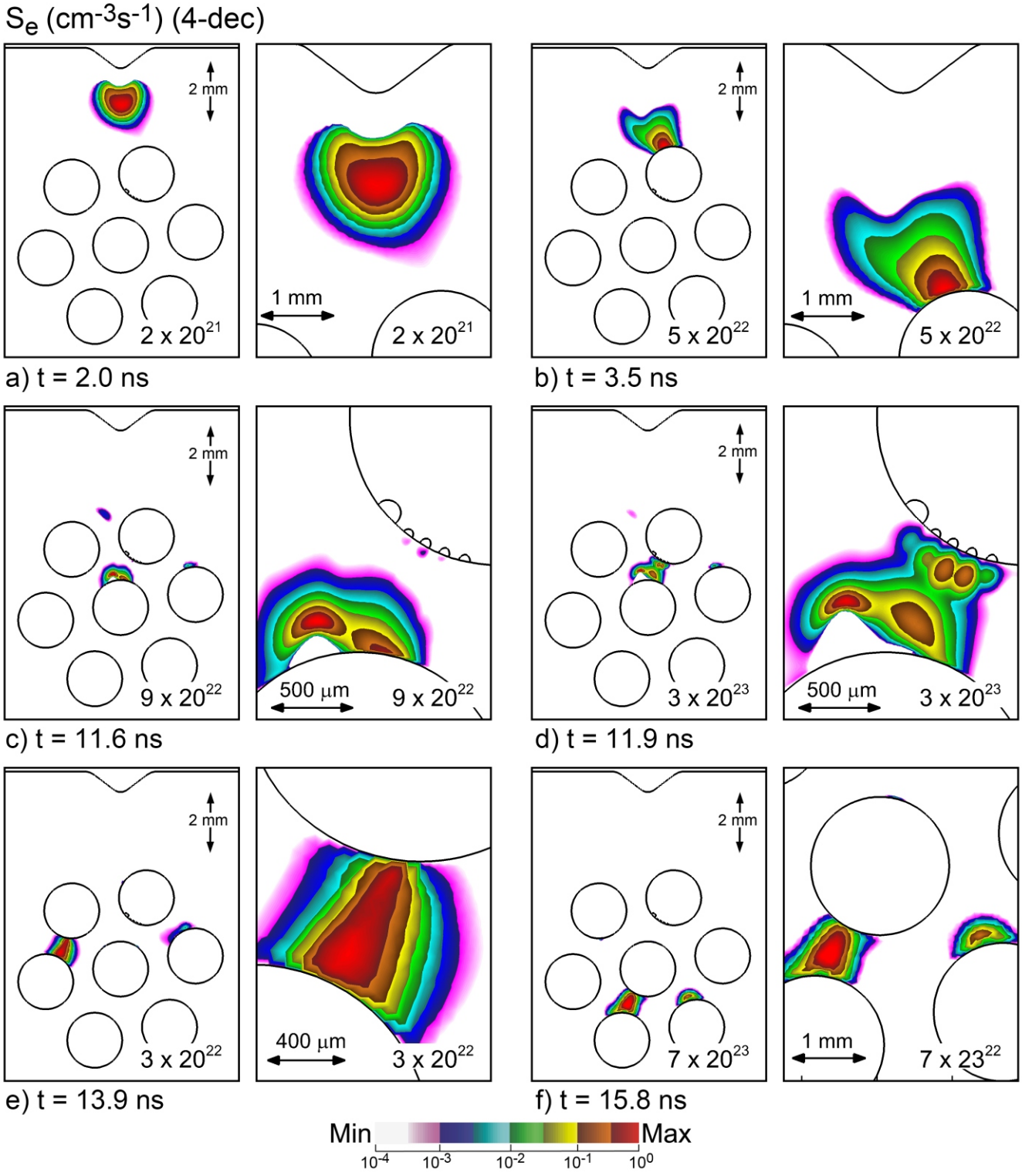

Kruszelnicki et al.
Figure 5 of 13

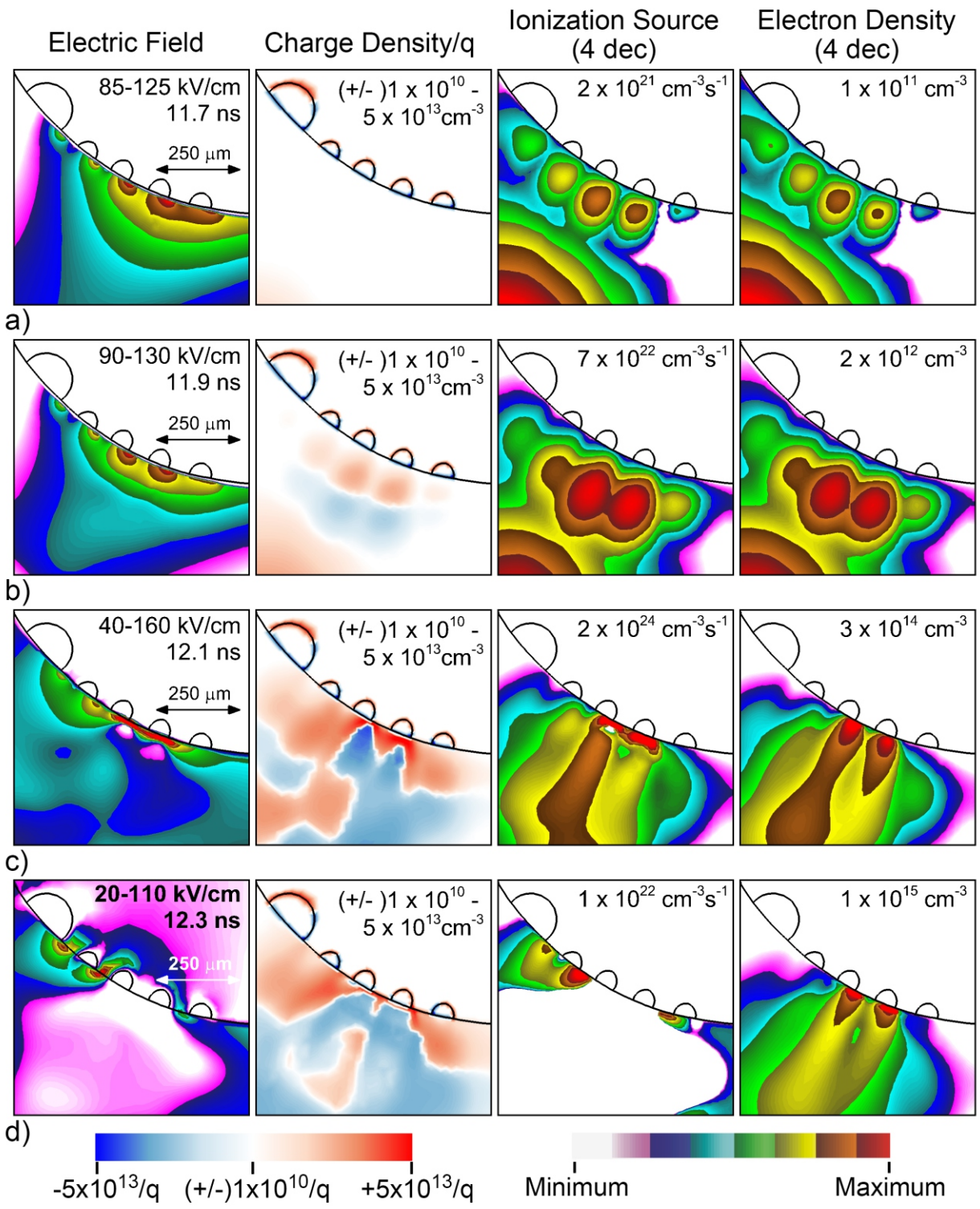

Kruszelnicki et al.
Figure 6 of 13

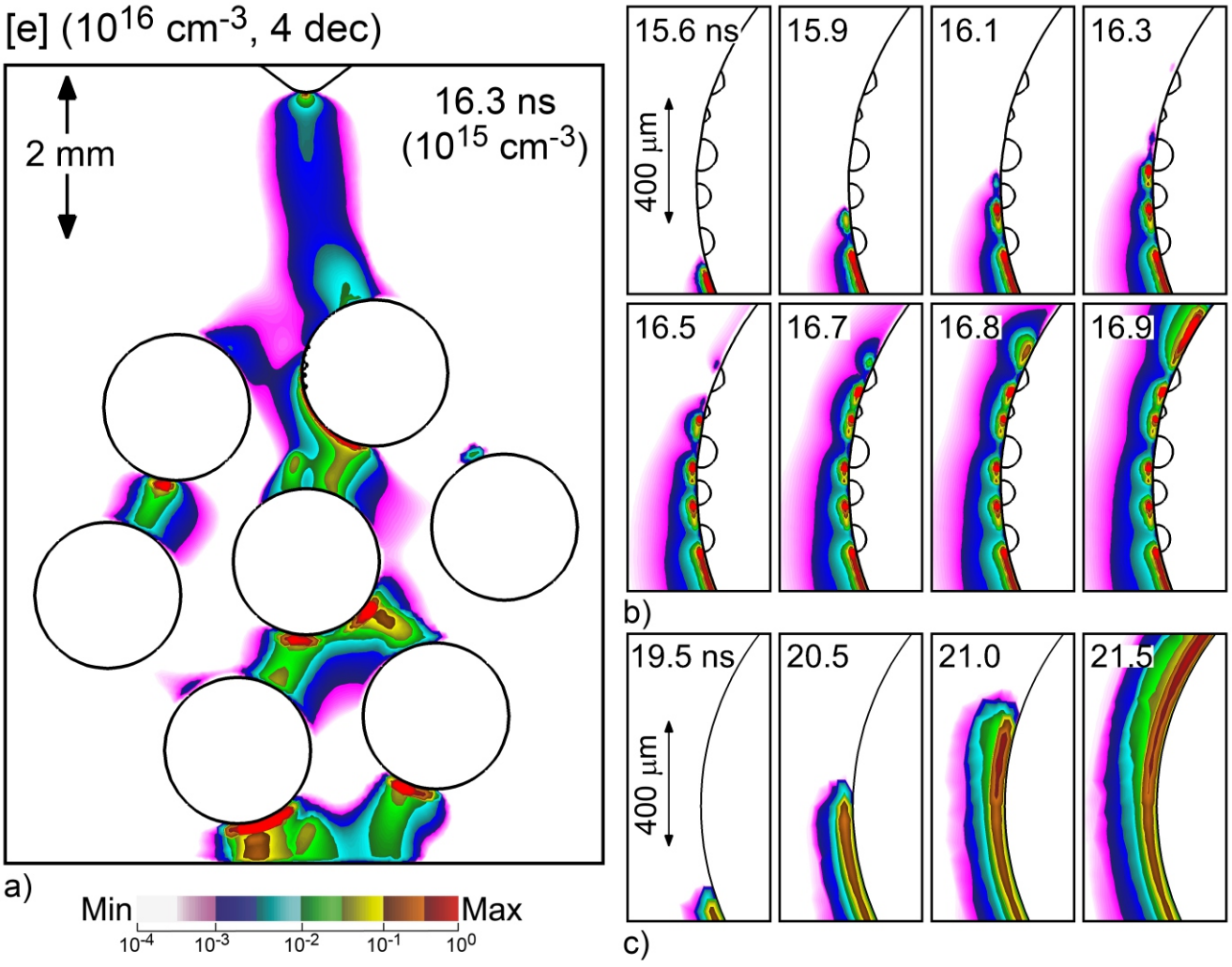
[e] (10^16 cm^-3, 4 dec)
2 mm
16.3 ns
(10^15 cm^-3)
a)
Min
Max
10^-4
10^-3
10^-2
10^-1
10^0
15.6 ns
15.9
16.1
16.3
400 µm
16.5
16.7
16.8
16.9
b)
19.5 ns
20.5
21.0
21.5
400 µm
c)

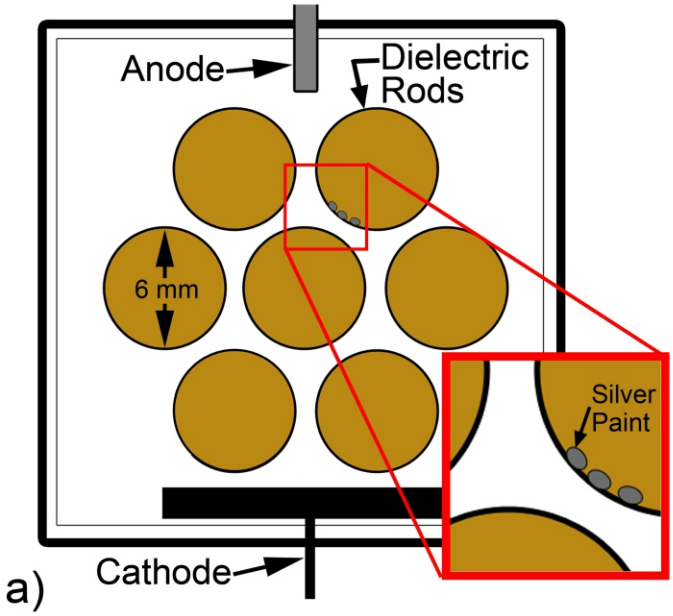

a)

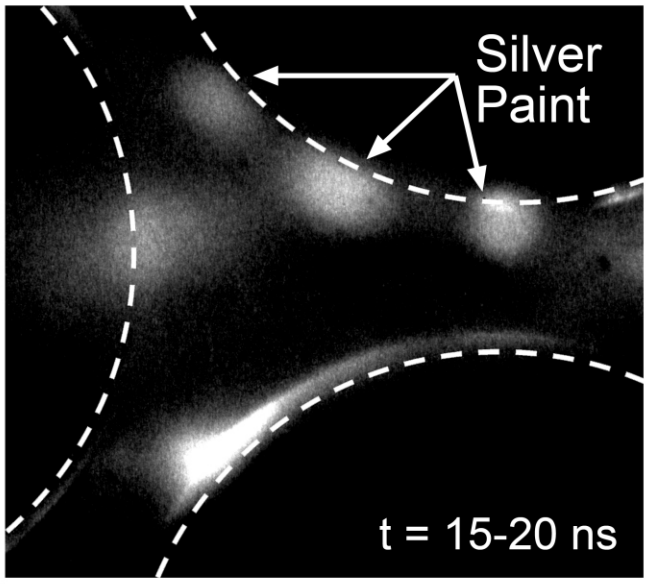

b)

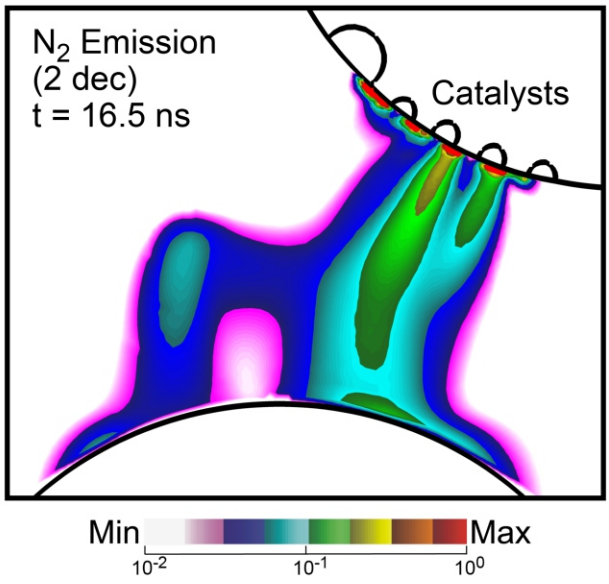

c)

Kruszelnicki et al.
Figure 8 of 13

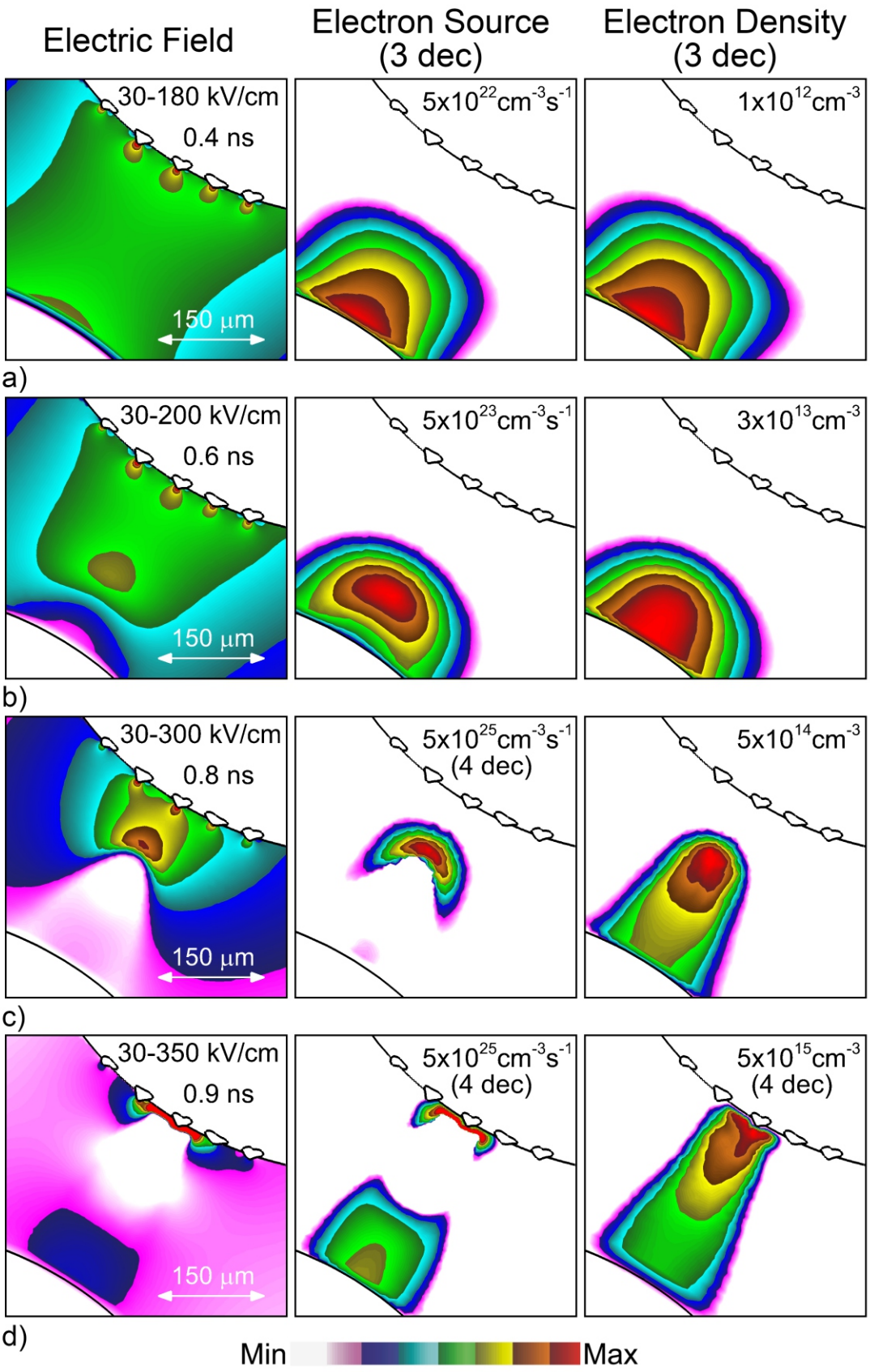

Kruszelnicki et al.
Figure 9 of 13

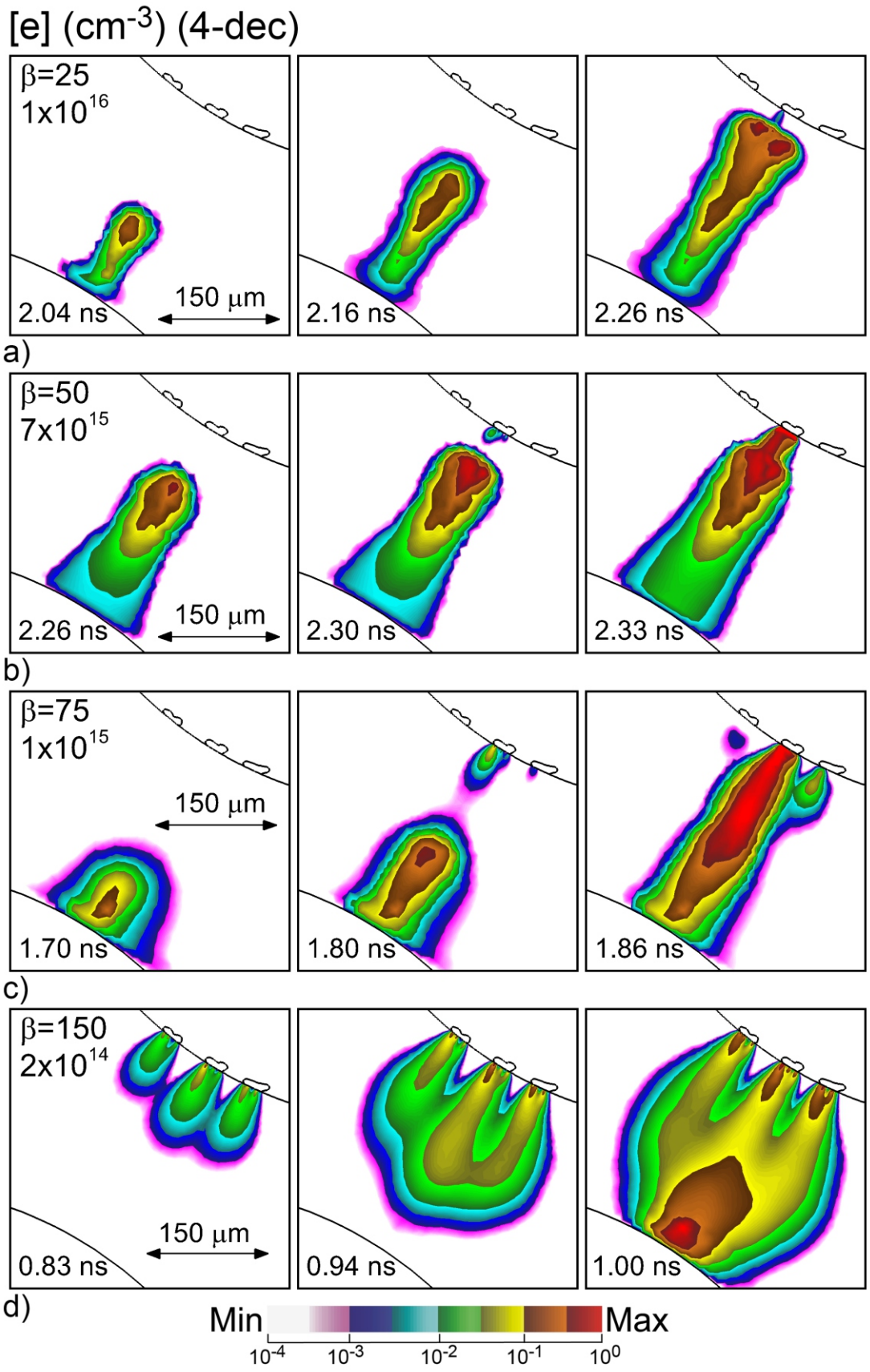

Kruszelnicki et al.
Figure 10 of 13

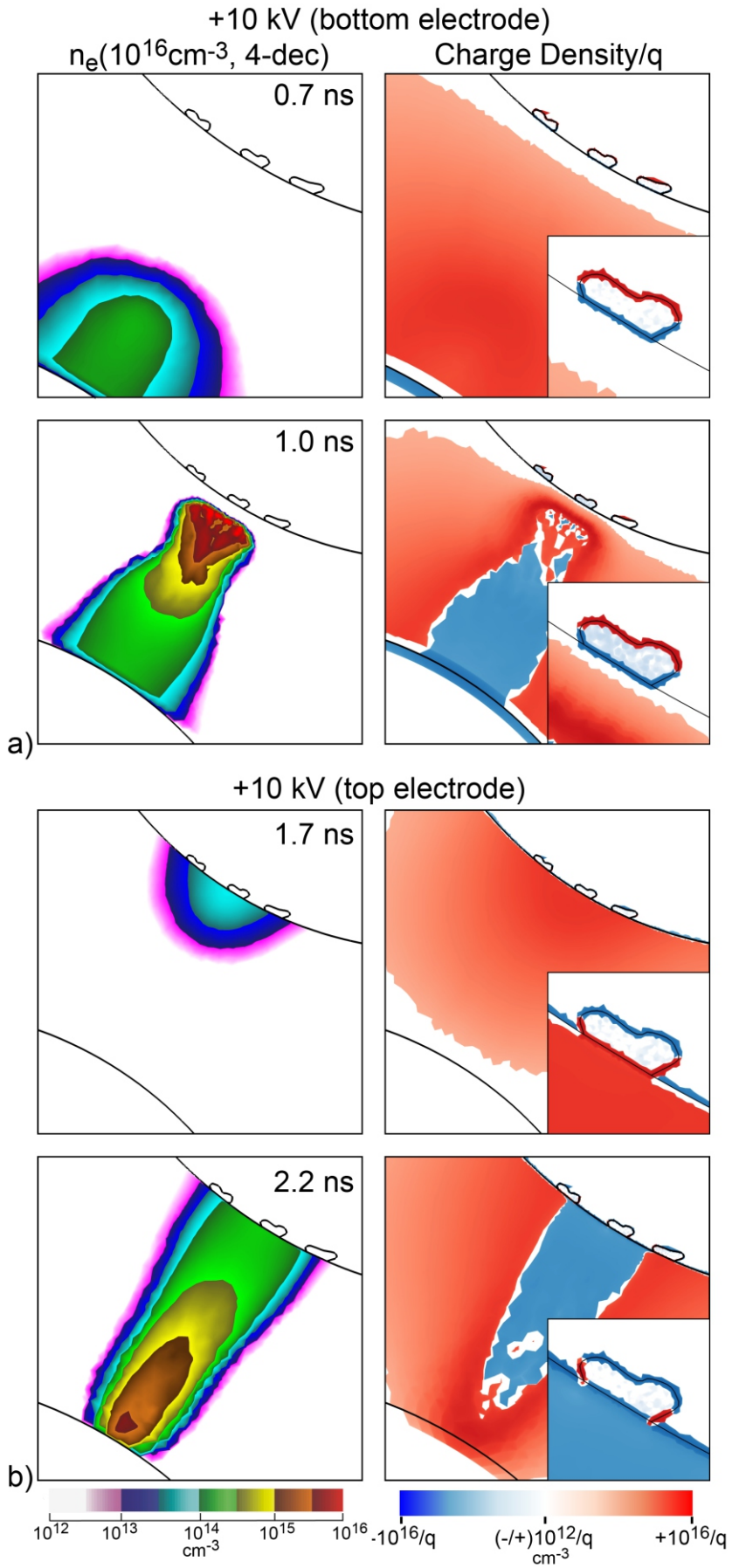

Kruszelnicki et al.
Figure 11 of 13

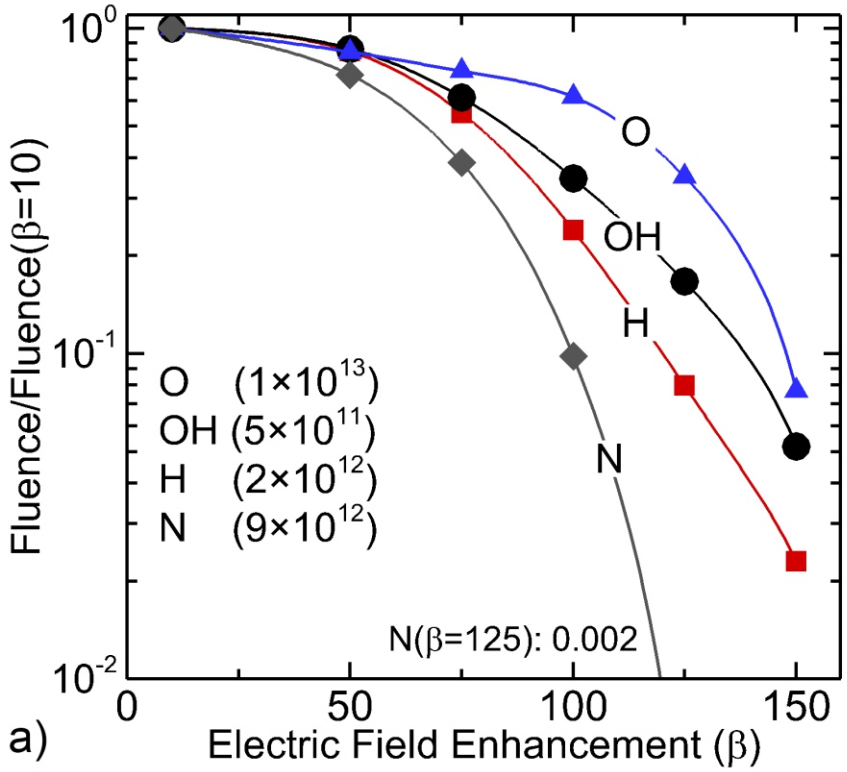

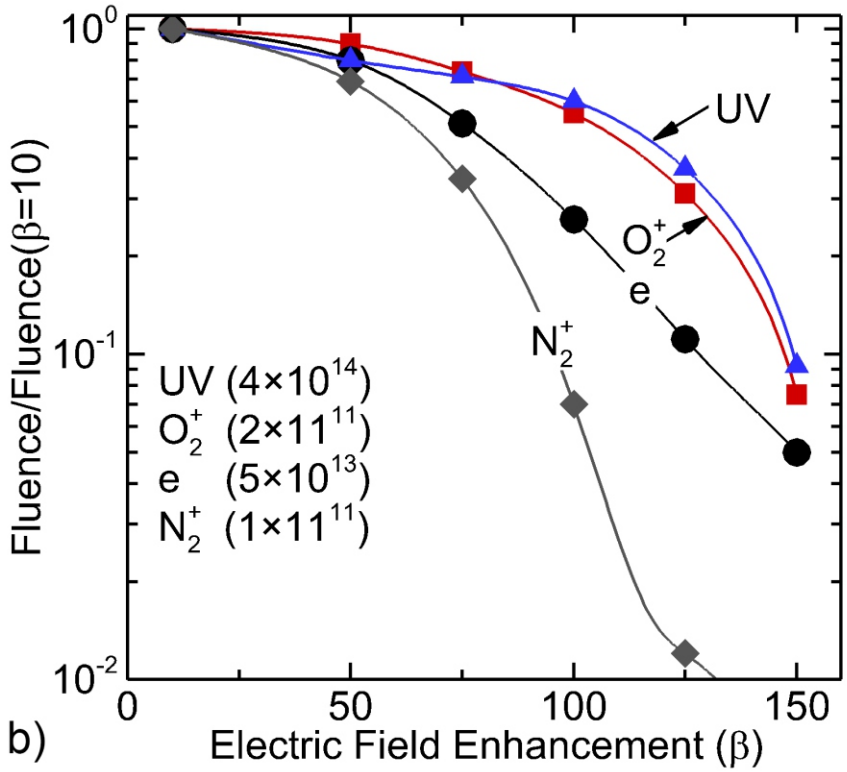

Kruszelnicki et al.
Figure 12 of 13

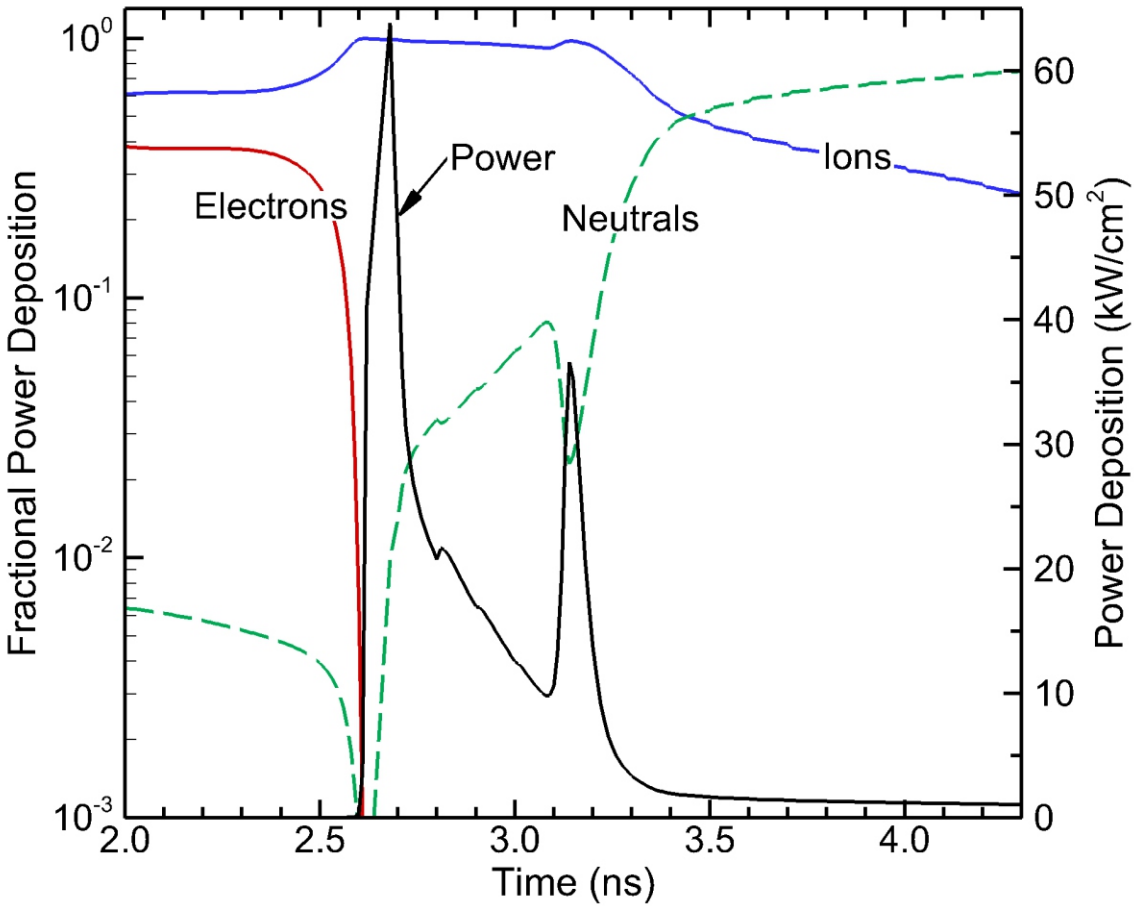

Kruszelnicki et al.
Figure 13 of 13